Journal of Magnetism and Magnetic Materials 603 (2024) 172262

Contents lists available at ScienceDirect

Journal of Magnetism and Magnetic Materials

journal homepage: www.elsevier.com/locate/jmmm

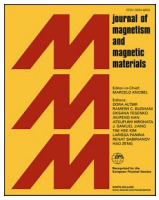

Research article

Correlation driven a novel spin-polarized hourglass loop in monolayer VCl_2

Weixi Zhang [a], Changhai Tian [a], Yong Li [a], Qianglin Hu [a], Yanchao She [a,*], Ping Li [b,c,**]

[a] Department of Physics and Electronic Engineering, Tongren University, Tongren 554300, China
[b] State Key Laboratory for Mechanical Behavior of Materials, School of Materials Science and Engineering, Xi'an Jiaotong University, Xi'an, Shaanxi 710049, China
[c] State Key Laboratory for Surface Physics and Department of Physics, Fudan University, Shanghai 200433, China

ARTICLE INFO

Keywords:
Monolayer materials
Spin-polarized hourglass loop
First-principles

ABSTRACT

Hourglass loop in two-dimensional (2D) systems is typically vulnerable against spin–orbit coupling (SOC). Here, we explore 2D systems with a type of spin-polarized nodal loop that is robust under SOC and characteristic of an hourglass-type dispersion. Through first-principles calculations, we identify the monolayer VCl_2 materials as a realistic material platform to realize an hourglass loop. There exist three phases, all of which are dynamically stable. For the γ-structure, as a new single spin hourglass loop material. It shows semiconducting and gapless properties in spin down and spin up channels, respectively. Moreover, it always exhibits an hourglass loop property in the absence and presence of SOC. It indicates that the hourglass has strong against SOC. Our work suggests a realistic material platform for investigating the novel physics associated with band crossings in 2D systems.

1. Introduction

Over the last decade, topological materials have attracted more and more attention due to their fascinating electronic band structures [1–11]. The research originated from drawing an insightful analogy between low-energy emergent fermions in condensed matters and fundamental particles in the relativistic quantum field theory [12,13]. The Dirac fermions were discovered [14], which can be described by the Dirac equation. Following, chiral Weyl fermions are predicated and ultimately spotted in low-energy condensed matter systems [15–17]. Apart from the zero-dimensional (0D) nodal points, the nontrivial band crossings may also take the form of one-dimensional (1D) nodal lines [18] or two-dimensional (2D) nodal surfaces [19] in three-dimensional (3D) systems.

Among the above-mentioned unconventional quasiparticles, a type of quasiparticle, whose band structure exhibits a unique hourglass-like dispersion in the Brillouin zone (BZ). It called an hourglass quasiparticle, and it has recently attracted widespread interest [20,21]. The hourglass network is almost located on the Fermi level and has a very clean band structure without interference bands nearby. Therefore, their intriguing properties may be easily studied in future experiments and are extremely important for transport properties. Afterward, theorists predicted hourglass fermions in 3D materials from two different bulk models [22,23]. Considering that the accidental band crossing is typically vulnerable against spin–orbit coupling (SOC), the intrinsically robust against SOC is especially important for the hourglass loop. For this reason, good candidate materials with fundamental band crossings are still limited. More importantly, the fundamental band crossing does not necessarily occur near the Fermi level, although they are guaranteed to exist in the band structure. Therefore, it is important to searching for an ideal hourglass fermion with the robust against SOC and band crossing appeared at the Fermi level.

As can be seen from the above considerations, the finding of two-dimensional topological materials is a challenging task. The requiring band crossings in such 2D materials to be robust to the SOC is even more challenging. Recently, Wan et al. studied the hourglass fermion from the perspective of 230 space groups [24]. However, so far, a few hourglass fermions have been observed in 2D real material systems.

In this work, based on symmetry analysis and first-principles calculations, we predicted an ideal hourglass fermion in two-dimensional penta-VCl_2. Our study found that the penta-VCl_2 has three phases, and their dynamics are stable. Analysis of band structure reveals an hourglass loop in spin up channel, while the spin down channel exhibits the properties of an insulator, indicating a spin-polarized hourglass loop. Interestingly, the hourglass loop exists with or without the SOC, showing that it is robust [25–27]. Importantly, the band crossings of the

* Corresponding author.
** Corresponding author at: State Key Laboratory for Surface Physics and Department of Physics, Fudan University, Shanghai 200433, China.
E-mail addresses: ycshe@xtu.edu.cn (Y. She), pli@xjtu.edu.cn (P. Li).

https://doi.org/10.1016/j.jmmm.2024.172262
Received 17 August 2023; Received in revised form 7 May 2024; Accepted 12 June 2024
Available online 16 June 2024

γ-structure appear at the Fermi level, which is the ideal hourglass loop. Our work offers guidance and a concrete material platform for exploring the robust hourglass loop in 2D materials.

2. Structures and computational methods

First, we used the Device Studio to build the structure. Then, to investigate the electronic and magnetic structures, density functional theory (DFT) calculations were carried out by using the projector augmented wave (PAW) method and the generalized gradient approximation (GGA), as implemented in the Vienna Ab initio Simulation Package (VASP) [28–31]. The projector augmented wave pseudopotential with an energy cutoff of 500 eV was adopted. Here, 16 × 16 × 1 and 24 × 24 × 1 Γ-centered k meshes are adopted for the structural optimization and the self-consistent calculations, respectively. The energy convergence criterion was set to be 10^{-6} eV for the electronic loop. The force on each atom is less than 0.01 eV/Å for the ionic loop. To investigate the structural stability, the phonon dispersion was calculated using a finite displacement method as implemented in the PHONOPY code [32]. In addition, to describe the strongly correlated 3d electrons of the V atom, the GGA + U method is used [33]. The onsite Coulomb repulsion U is varied between 0 and 3 eV for V. To explore the topological properties, we projected the Bloch wave function into maximally localized Wannier functions (MLWFs) [27,34,35] derived from the V d orbitals and made use of the WANNIERTOOLS package [36,37]. Moreover, the surface spectrum was calculated in a half-infinite boundary condition using the Green's function method [35].

3. Result and discussion

3.1. Structure and stability

Although the experiment successfully prepared 2H phase hexagonal VCl_2 [36], the penta-VCl_2 has not been reported so far. By comparing the structure of penta-$PdSe_2$, we notice that one planar structure and two different types of buckling can exist in a 2D material. Therefore, we define three structures as α-structure, β-structure, and γ-structure, as shown in Fig. 1. In the α-structure, coplanar Cl atoms are paired to create Cl-Cl dimers, whereas in the β-structure, Cl atoms are interspersed by V atoms. Transitioning from the α-structure to the β-structure and γ-structure is achieved by interchanging the z coordinates of the Cl1 and Cl2 atoms, as depicted in Fig. 1(d).

As shown in Fig. 1(c), it is the optimized structure of γ-structure VCl_2 (planar structure). The γ-structure of VCl_2 features coplanar arrangements of V and Cl atoms, forming a Cairo pentagonal tiling pattern. The lattice has a tetragonal symmetry and belongs to the P4/mbm space group, maintaining an inversion symmetry and a D_{4h} point group symmetry. Each primitive cell comprises two V atoms and four Cl atoms, and the equilibrium lattice constants are a = b = 6.46 Å. Although the γ-structure VCl_2 is energetically higher than the α-structure and β-structure (see Fig. 1(d)), it does not mean that it cannot exist stably. As shown in Fig. 1(d), the energy barrier between gamma and alpha phase is 1.837 eV.

To investigate the structural stability of three VCl_2 structures, we first calculate the phonon dispersion by 3 × 3 × 1 supercell. The energy

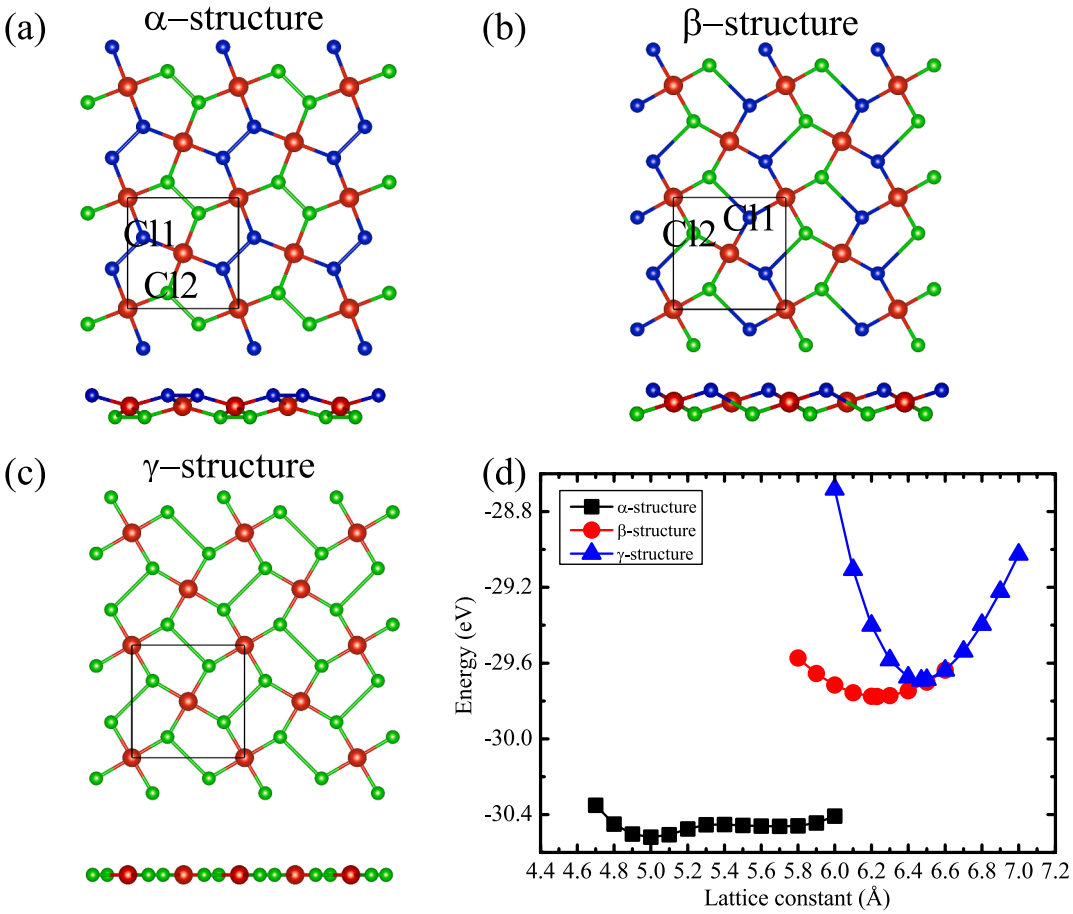

Fig. 1. Top and side views of (a) α-structure, (b) β-structure, and (c) γ-structure penta-VCl_2, where the bottom and top layers of Cl atoms are shown by green and blue balls, respectively. (d) The graph illustrates the total energy variation of penta-VCl_2 monolayers for various structures against changes in the lattice constant. The insets provide optimized depictions of the penta-VCl_2 monolayer with the α-structure. (For interpretation of the references to colour in this figure legend, the reader is referred to the web version of this article.)

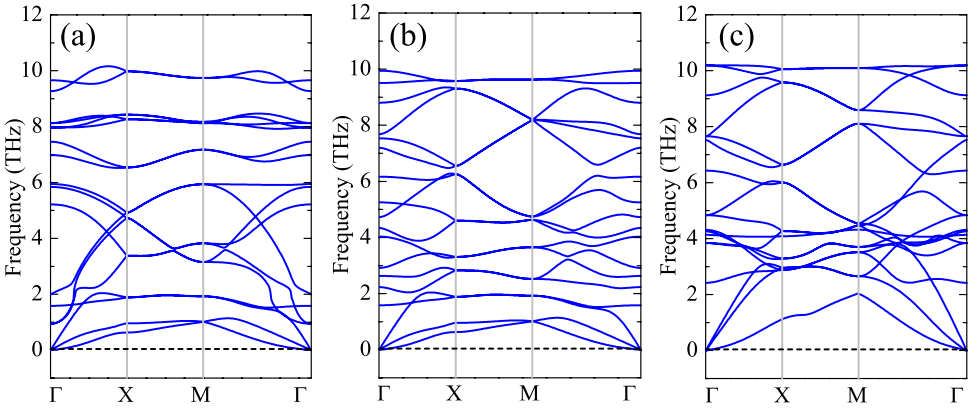

Fig. 2. The calculated phonon dispersion of (a) *α*-structure, (b) *β*-structure, and (c) *γ* −structure penta-VCl_2.

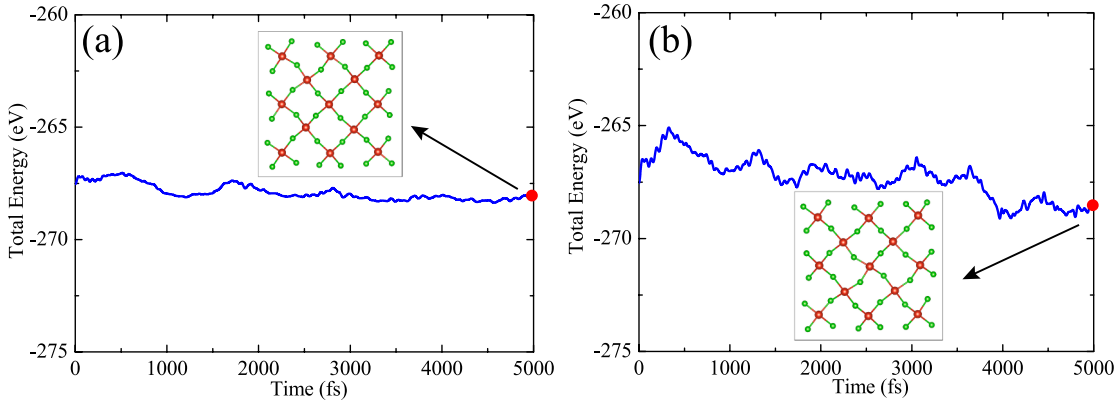

Fig. 3. Total energy fluctuations of the *γ*-structure penta VCl_2 during 5 ps AIMD simulation at 100 K (a), and 300 K (b).

convergence criterion was set to be 10^{-8} for the electronic loop. The results are shown in Fig. 2. There is no imaginary frequency throughout the entire BZ, indicating their dynamical stability. Moreover, we use ab initio molecular dynamics (AIMD) simulations to prove under different temperatures thermal stability of *γ*-VCl_2. In contrast to the MLIP package [38,39], both of them can well characterize the dynamic stability of the material. The MLIP package is more suitable for large-scale machine learning molecular dynamics, while the AIMD is more suitable for the study of small number systems with high precision. As depicted in Fig. 3, the lattice structure remains largely unchanged for *γ*-VCl_2 after annealing at both 100 K and 300 K for a duration of 5 ps. It indicates that thermodynamics is stable.

3.2. Magnetic properties and Curie temperature

To ascertain the magnetic characteristics of the three VCl_2 structures, magnetic exchange energies were computed for various magnetic states, encompassing nonmagnetic (NM), ferromagnetic (FM), and three antiferromagnetic (AFM) configurations, as illustrated in Fig. 4(a-d). The investigation of magnetic, band structure, and topological properties was conducted employing the density functional theory (DFT) + U method, with a focus on the V 3d orbitals. Diverse effective Hubbard energy values, such as 0 and 3 eV, were taken into consideration in our calculations. For three structures, the magnetic ground state is always the FM state under any different U_{eff}.

In the context of intrinsic ferromagnetic (FM) states, magnetic anisotropy serves as a significant indicator for establishing the magnetic orientation at low temperatures relative to the lattice structure. It is closely tied to the thermal stability of magnetic data storage. Hence, the magnetocrystalline anisotropy energy (MAE) was defined as $E_{MAE} = E_{100} - E_{001}$, where E_{100} and E_{001} represent the total energy in (1 0 0) and (0 0 1) orientation. Here, we give the MAE values for $U_{eff} = 2$ eV to be −0.85 meV (α-structure), 0.21 meV (β-structure), and −1.59 meV (γ-structure), indicating the magnetization along the x-axis for the α-structure and γ-structure, while the magnetization along the z-axis for the β-structure.

To assess the Curie temperature of ferromagnetic (FM) VCl_2, we perform Monte Carlo simulations utilizing a 2D Heisenberg model. The spin Hamiltonian of VCl_2 monolayer has a general form

$$H = E_0 + \sum_{\langle i,j \rangle} J_1 S_i \cdot S_j + \sum_{\langle i,k \rangle} J_2 S_i \cdot S_k + \sum_{\langle i,l \rangle} J_3 S_i \cdot S_l \quad (1)$$

where J_1, J_2, and J_3 are first nearest-neighbor (NN) exchange parameter, second NN exchange parameter, and third NN exchange parameter. S_i, S_j, S_k, and S_l represent the magnetic moments at sites *i*, *j*, *k*, and *l*, respectively. E_0 is energy independent of magnetism. A 2 × 2 × 1 supercell contains eight V atoms. For the FM phase (see Fig. 4(a)), there are 16 first NN interactions with each other, 16 s NN interactions with each other and 10 third NN interaction with each other in the 2 × 2 × 1 supercell. Therefore, the total energy of the FM state is expressed as

$$E_{FM} = E_0 + (16J_1 + 16J_2 + 10J_3)S^2, \quad (2)$$

For the AFM1 phase, the nearest neighbors are all AFM coupling, while the second NN and third NN are FM coupling. Thus, the total energy of the AFM1 state is expressed as

$$E_{AFM1} = E_0 + (-16J_1 + 16J_2 + 10J_3)S^2, \quad (3)$$

For the AFM2 phase, the nearest neighbor has eight FM couplings and eight AFM couplings. Thus, the nearest neighbor interaction is cancelled out. Similarly, the nearest neighbors are also cancelled out. Only the three-neighbor interaction is preserved. Since the third nearest neighbor

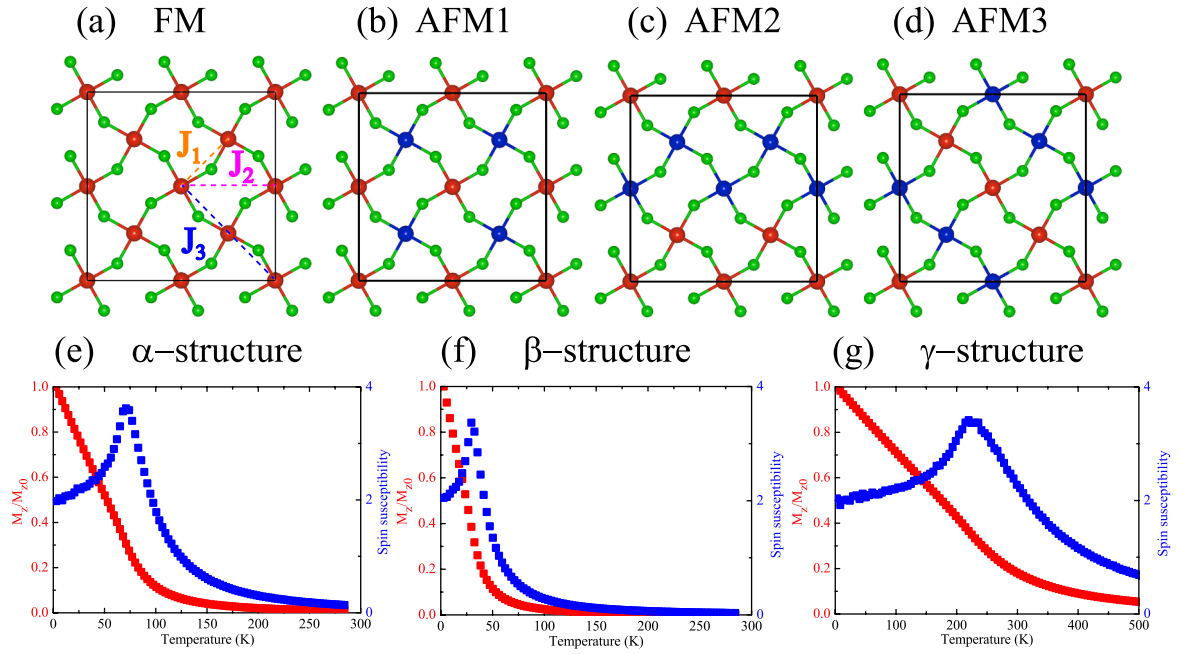

Fig. 4. Top view of the four magnetic configurations, namely (a) ferromagnetic (FM), (b) antiferromagnetic (AFM1), (c) antiferromagnetic2 (AFM2), and (d) antiferromagnetic3 (AFM3), where the red (blue) circles denote the up (down) spins. Monte Carlo simulations on the magnetic moment (red) and spin susceptibility (blue) as a function of temperature for (e) α-structure, (f) β-structure, and (g) γ-structure penta-VCl_2. (For interpretation of the references to colour in this figure legend, the reader is referred to the web version of this article.)

is AFM coupling, the expression is

$$E_{AFM2} = E_0 - 10J_3S^2, \tag{4}$$

For the AFM3 phase, the nearest neighbor has eight FM couplings and eight AFM couplings. Thus, the nearest neighbor interaction is cancelled out. The second and third nearest neighbors are FM and AFM coupling, respectively. Hence, the expression is

$$E_{AFM3} = E_0 + (-16J_2 + 10J_3)S^2, \tag{5}$$

By mapping the DFT energies to the Heisenberg model, the calculated exchange coupling parameters are $J_1 = -7.41$ meV, $J_2 = -0.02$ meV, and $J_3 = -0.83$ meV for the α-structure; J_1 = -3.81 meV, $J_2 = -0.08$ meV, and $J_3 = 0.09$ meV for the β-structure; $J_1 = -27.94$ meV, $J_2 = -0.41$ meV, and $J_3 = 10.44$ meV for the γ-structure. It is important to highlight that the value of J_2 is significantly smaller in magnitude compared to J_1 and J_3. The Curie temperature holds crucial significance as it allows for the experimental observation of topological properties. The Monte Carlo simulations are executed on an 80 × 80 lattice grid over a duration of 10^6 steps, each with a step size of 3 K. The obtained Curie temperature of three structures are 68 K (α-structure), 27 K (β-structure), and 220 K (γ-structure), as shown in Fig. 4(e-g). The spin susceptibility is considered to improve the estimation accuracy. Given that Monte Carlo simulations of Heisenberg models often result in an overestimation of the actual Curie temperature, the computed value of T_C can be considered as an upper limit.

3.3. Electronic band structure

Now we research the electronic properties of three structures. The spin-polarized band structures of the VCl_2 monolayer are shown in Fig. 5. For the α-structure and β-structure, as the U_{eff} value increases, a phase transition from half-metal to insulator occurs. For the γ-structure, regardless of any U_{eff} value, it always reflects half-metal. Of particular interest, when the effective Hubbard parameter (U_{eff}) surpasses 0, an intriguing observation emerges: multiple band crossings are apparent near the Fermi level within the spin-up channel, while the spin-down channel demonstrates semiconducting behavior, as depicted in Fig. 5 (i-l). These band crossing points align along the Γ-X and Γ-M directions. Moreover, accounting for symmetry effects unveils additional band crossing points across the entire Brillouin zone (BZ). It may be an hourglass loop.

First, compared with many examples for 3D hourglass loop materials, 2D hourglass loop materials are much fewer. Although there are quite a few theoretical proposals of 3D hourglass loop materials [25,26], none have been experimentally confirmed so far. Moreover, GaTeI and Bi/Cl-SiC(1 1 1) are not ideal, because the hourglass loop is away from the Fermi level. More importantly, the SOC effect change the hourglass loop and opens gap. In comparison, the hourglass loop in the γ-structure penta-VCl_2 is more robust due to the negligible SOC.

After the inclusion of the SOC, the easy magnetization direction of the α and γ–structure is the x-axis, while the easy magnetization axis of the β-structure is the z-axis for U = 2 eV. Therefore, we calculated the SOC band in the easy magnetization direction. As shown in Fig. 6, the band structure is almost unchanged compared to the spin-polarized band structure. The hourglass loop does not open the band gap. Therefore, VCl_2 presents a robust platform to investigate the hourglass loop.

To delve deeper into the band characteristics of VCl_2, plotting the orbital-resolved band structure becomes imperative, as illustrated in Fig. 7. In the case of the γ-structure penta-VCl_2, the hourglass feature primarily originates from the contributions of the d_{xz} and d_{yz} orbitals of the V atoms. These d_{xz} and d_{yz} orbitals exhibit degeneracy at the Γ point, which holds D_{4h} symmetry. This degeneracy results in the formation of a bonding π state and an antibonding π* state below and above the Fermi level, respectively. When tracing the path along Γ-X and Γ-M, the initially degenerate d_{xz} and d_{yz} bands undergo a splitting into two distinct branches due to a reduction in symmetry to C_{2v}. Within this context, the lower π band and the higher π* band intersect, giving rise to the formation of the hourglass loop. This intersection occurs because these bands belong to different symmetry representations, which inhibits their hybridization. Consequently, the occurrence of band crossings within the spin up channel becomes inevitable.

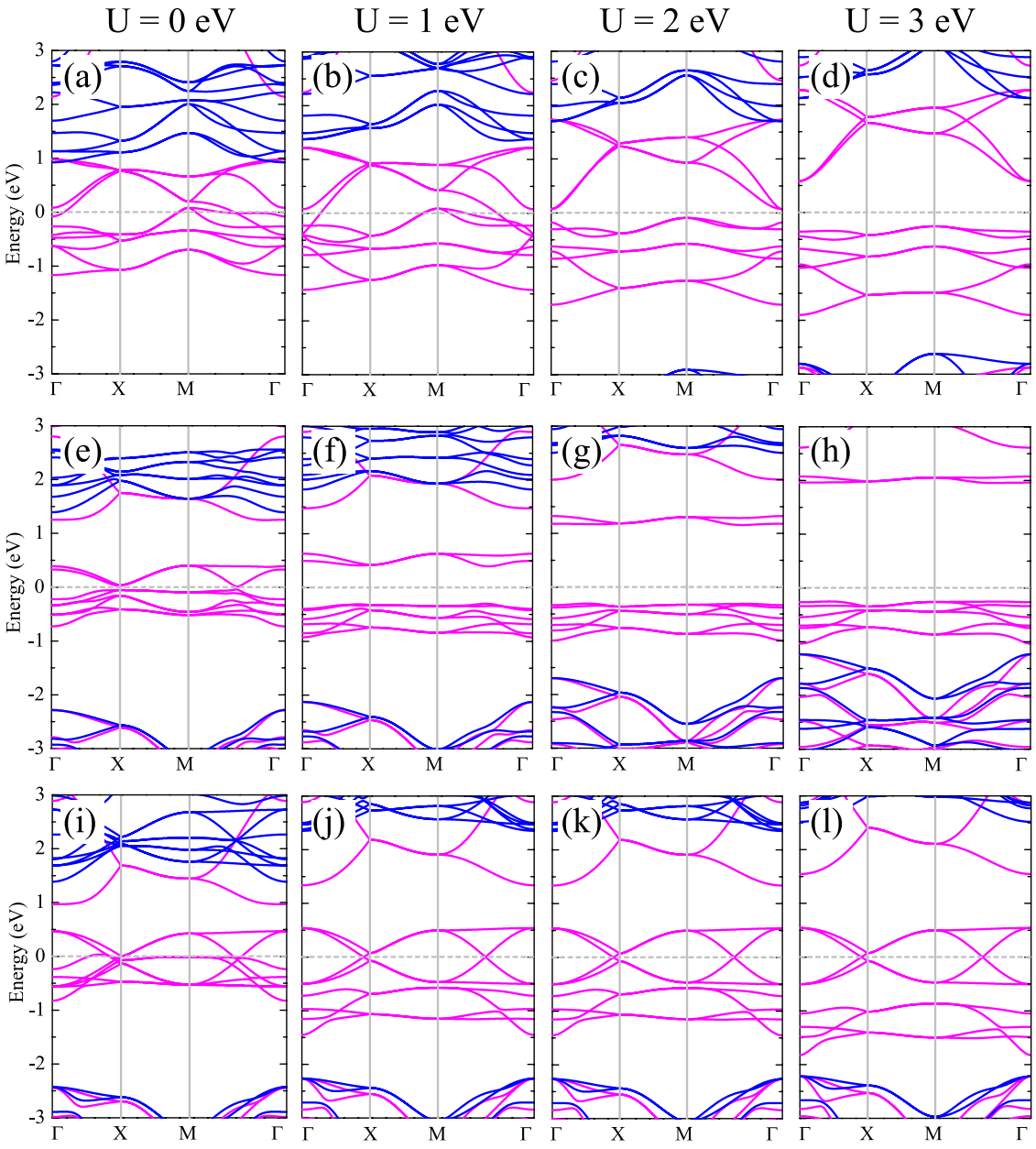

Fig. 5. Spin-polarized band structures for the different U values. The first line, the second line, and the third line are α-structure, β-structure, and γ-structure penta-VCl_2. Moreover, the four columns are U = 0 eV, U = 1 eV, U = 2 eV, and U = 3 eV, respectively. The magenta and blue curves correspond to the spin up and spin down channels, respectively. (For interpretation of the references to colour in this figure legend, the reader is referred to the web version of this article.)

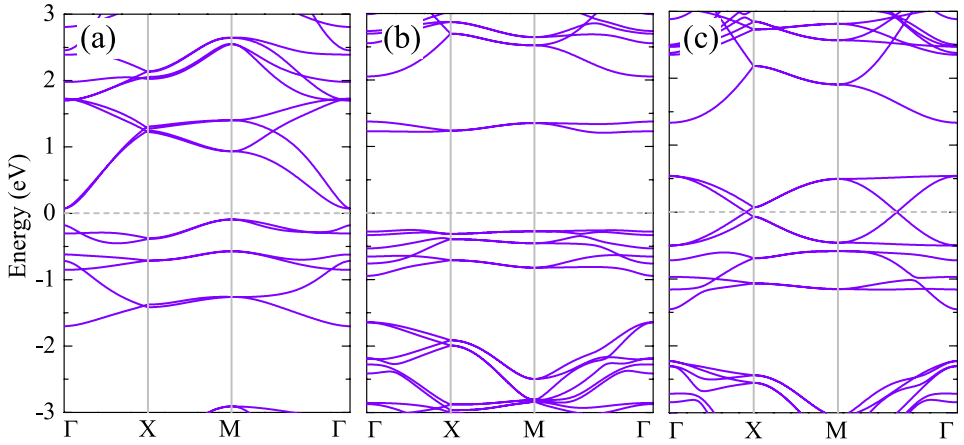

Fig. 6. Band structures with SOC for U = 2 eV, (a) α-structure while the direction of the magnetic moment is in the x direction, (b) β-structure while the direction of the magnetic moment is in the z direction, and (c) γ-structure while the direction of the magnetic moment is in the x direction.

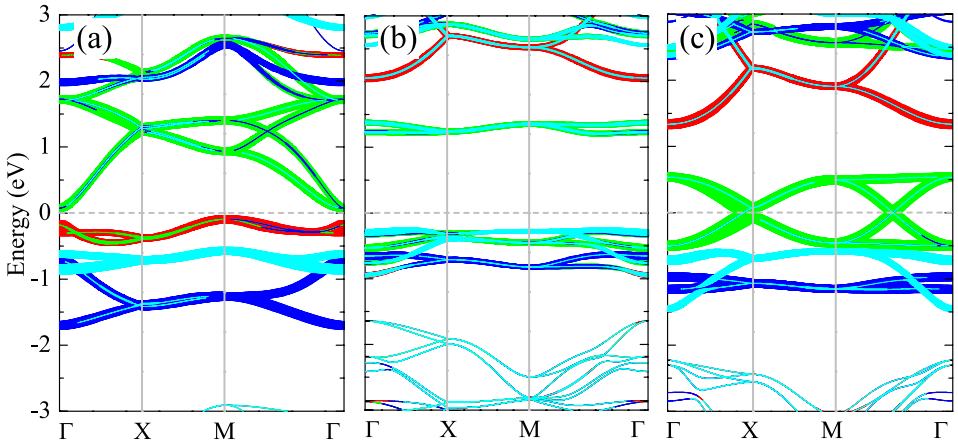

Fig. 7. Energy and k contributions of V-d-resolved to the bands structure with SOC for (a) α-structure, (b) β-structure, and (c) γ-structure penta-VCl_2. The red, green, dark blue, and light blue indicate the contributions of d_{xy}, $d_{xz}+d_{yz}$, d_{z2} and d_{x2-y2} orbitals of V atoms, respectively. (For interpretation of the references to colour in this figure legend, the reader is referred to the web version of this article.)

3.4. Onsite correlation tunable topological properties

To examine the alterations in the band structure and topological phase as the strength of the onsite Coulomb repulsion U is modified, we present the band structures computed without taking spin–orbit coupling (SOC) into account in Fig. 5. Interestingly, when the U_{eff} value is greater than 0, it may be an hourglass loop for γ-structure. In order to comprehensively comprehend the band characteristics of the γ-structure penta-VCl_2 across the entire Brillouin zone (BZ), it is essential to visualize the 3D band structure. By examining the 3D band structure in Fig. 8 (a), it becomes evident that the distinctive degenerate points associated with the hourglass cone exclusively appear along the k path, specifically along the directions of Γ-X and Γ-M. They belong to the same hourglass loop centered around the Γ point.

The presence of an hourglass loop frequently gives rise to surface states, as demonstrated in previous studies [20,40]. As depicted in Fig. 8 (b), we present the plotted surface state, revealing the emergence of such a state. Notably, this characteristic bears resemblance to the surface state observed in the hourglass Dirac chain material ReO_2 [41].

Notably, the neck point within the hourglass dispersion is required to form a closed Dirac loop encircling the Γ point, as depicted in Fig. 8(c). Our DFT results indeed validate this expectation, as illustrated in Fig. 8 (d). One potential explanation for this phenomenon can be provided as follows: the γ-structure of VCl_2 possesses a horizontal mirror plane M_z that runs parallel to the lattice. In the absence of SOC, the four bands composing the hourglass loop exhibit distinct eigenvalues under the operation of the horizontal mirror plane M_z. The wave functions associated with the d_{xz} and d_{yz} orbitals possess differing even and odd

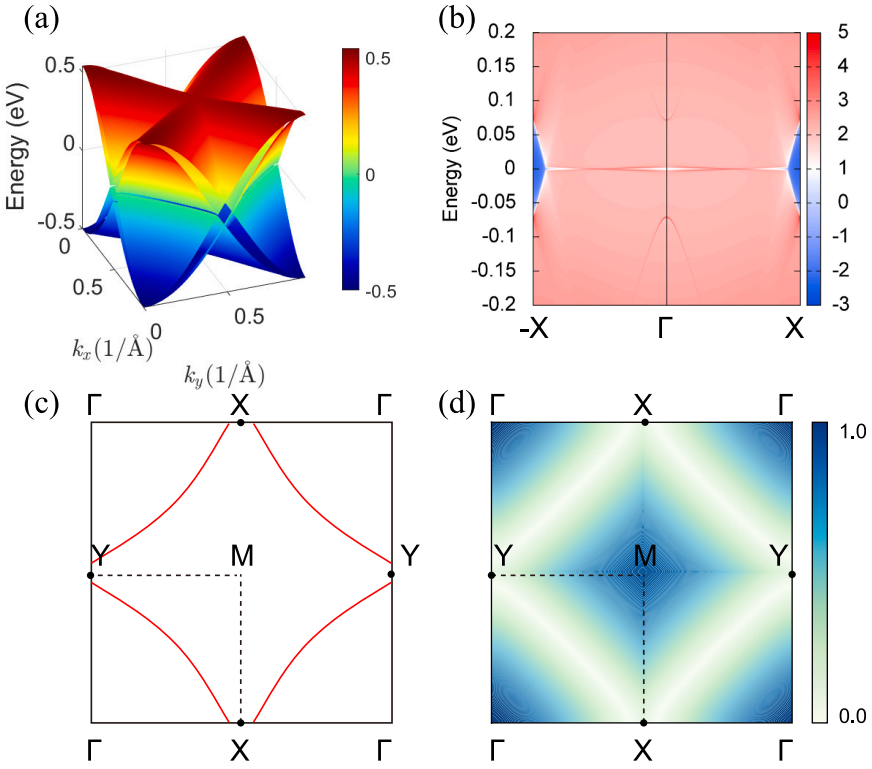

Fig. 8. (a) 3D band structure with SOC for γ-structure VCl_2. (b) The calculated chiral edge state of a semi-infinite sheet of VCl_2. (c) Schematic figure showing the neck point of the hourglass dispersion. (d) The energy difference of γ-structure VCl_2 in the 3D BZ, where the white line indicates the location of the hourglass loop.

behavior under M_z. Consequently, these four bands intersect to form the hourglass loop. Our analysis conclusively establishes that this hourglass loop is fundamental and entirely governed by the symmetry inherent in the space group.

4. Conclusion

In summary, by using first-principles calculations, we discover a new 2D material, pentagonal VCl_2. There exist three phases, all of which are dynamically stable. We find the first of spin-polarized hourglass loop in 2D material. γ-structure VCl_2, which bridges hourglass loop materials and spintronics, exhibits many unique properties including large spin polarization and robust topological properties. The Curie temperature estimated from Monte Carlo simulations is about 230 K. Most importantly, the hourglass loop is intrinsic and does not require any external conditions in experiments such as strain, magnetic field, or electric field. Our findings will provide an excellent platform for designing new topological spintronics devices.

CRediT authorship contribution statement

Weixi Zhang: Funding acquisition, Investigation, Writing – original draft, Writing – review & editing. **Changhai Tian:** Investigation. **Yong Li:** Investigation. **Qianglin Hu:** Data curation, Formal analysis. **Yanchao She:** Funding acquisition, Software, Validation. **Ping Li:** Conceptualization, Funding acquisition, Investigation, Resources, Writing – review & editing.

Declaration of competing interest

The authors declare that they have no known competing financial interests or personal relationships that could have appeared to influence the work reported in this paper.

Data availability

No data was used for the research described in the article.

Acknowledgments

This work is supported by the National Natural Science Foundation of China (Grants No. 12064038, 12165016, and 12004295), the Natural Science Foundation of Guizhou Provincial Provincial Education Department, China (Grant No. ZK[2021]034 and ZK[2022]558), and the PhD Starting Fund program of TongRen University (Grant No. trxyDH2223). P. Li also acknowledge supports from the China's Postdoctoral Science Foundation funded project (Grant No. 2022M722547), the Fundamental Research Funds for the Central Universities (xxj03202205), and the Open Project of State Key Laboratory of Surface Physics (No. KF2024_02).

References

[1] M.Z. Hasan, C.L. Kane, Topological insulators, Rev. Mod. Phys. 82 (2010) 3045, https://doi.org/10.1103/RevModPhys.82.3045.
[2] X.L. Qi, S.C. Zhang, Topological insulators and superconductors, Rev. Mod. Phys. 83 (2011) 1057, https://doi.org/10.1103/RevModPhys.83.1057.
[3] A. Bansil, H. Lin, T. Das, Colloquium: Topological band theory, Rev. Mod. Phys. 88 (2016) 021004, https://doi.org/10.1103/RevModPhys.88.021004.
[4] P. Li, X. Li, W. Zhao, H. Chen, M.X. Chen, Z.X. Guo, J. Feng, X.G. Gong, A. H. MacDonald, Topological Dirac states beyond π-orbitals for silicene on SiC (0001) surface, Nano Lett. 17 (2017) 6195, https://doi.org/10.1021/acs.nanolett.7b02855.
[5] W.X. Zhang, Y. Li, Y.C. She, Two-dimensional transition-metal halide $CoBr_3$ with spin-polarized Dirac cone, Phys. Chem. Chem. Phys. 21 (2019) 17740, https://doi.org/10.1039/C9CP03337H.
[6] P. Li, T.Y. Cai, Two-dimensional transition-metal oxides Mn_2O_3 realized the quantum anomalous hall effect, J. Phys. Chem. C. 124 (2020) 12705, https://doi.org/10.1021/acs.jpcc.0c01308.
[7] P. Li, T.Y. Cai, Fully spin-polarized quadratic non-Dirac bands realized quantum anomalous Hall effect, Phys. Chem. Chem. Phys. 22 (2020) 549, https://doi.org/10.1039/C9CP05132E.
[8] P. Li, Y. Ma, Y. Zhang, Z.X. Guo, Room temperature quantum anomalous hall insulator in a Honeycomb-Kagome lattice, Ta_2O_3, with huge magnetic anisotropy energy, ACS Appl. Electron. Mater. 3 (2021) 1826, https://doi.org/10.1021/acsaelm.1c00085.
[9] P. Li, X. Yang, Q.S. Jiang, Y.Z. Wu, W. Xun, Built-in electric field and strain tunable valley-related multiple topological phase transitions in VSiXN4(X = C, Si, Ge, Sn, Pb) monolayers, Phys. Rev. Mater. 7 (2023) 064002, https://doi.org/10.1103/PhysRevMaterials.7.064002.
[10] P. Li, C. Wu, C. Peng, M. Yang, W. Xun, Multifield tunable valley splitting in two-dimensional MXene Cr_2COOH, Phys. Rev. B 108 (2023) 195424, https://doi.org/10.1103/PhysRevB.108.195424.
[11] W. Xun, C. Wu, H. Sun, W. Zhang, Y.Z. Wu, P. Li, Coexisting magnetism, ferroelectric, and ferrovalley multiferroic in stacking-dependent two-dimensional materials, Nano Lett. 24 (2024) 3541, https://doi.org/10.1021/acs.nanolett.4c00597.
[12] L. Fu, C.L. Kane, Superconducting proximity effect and Majorana fermions at the surface of a topological insulator, Phys. Rev. Lett. 100 (2008) 096407, https://doi.org/10.1103/PhysRevLett.100.096407.
[13] X. Wan, A.M. Turner, A. Vishwanath, S.Y. Savrasov, Topological semimetal and Fermi-arc surface states in the electronic structure of pyrochlore iridates, Phys. Rev. B 83 (2011) 205101, https://doi.org/10.1103/PhysRevB.83.205101.
[14] K.S. Novoselov, A.K. Geim, S.V. Morozov, D. Jiang, M.I. Katsnslson, I.V. Grigorieva, S.V. Dubonos, A.A. Firsov, Two-dimensional gas of massless Dirac fermions in graphene, Nature 438 (2005) 197, https://doi.org/10.1038/nature04233.
[15] H. Weyl, Quantenmechanik und Gruppentheorie, Z. Phys. 46 (1927) 1–46, https://doi.org/10.1007/bf02055756.
[16] G. Xu, H. Weng, Z. Wang, X. Dai, Z. Fang, Chern semimetal and the quantized anomalous hall effect in $HgCr_2Se_4$, Phys. Rev. Lett. 107 (2011) 186806, https://doi.org/10.1103/PhysRevLett.107.186806.
[17] B.Q. Lv, H.M. Weng, B.B. Fu, X.P. Wang, H. Miao, J. Ma, P. Richard, X.C. Huang, L. X. Zhao, G.F. Chen, Z. Fang, X. Dai, T. Qian, H. Ding, Experimental discovery of Weyl semimetal TaAs, Phys. Rev. X 5 (2015) 031013, https://doi.org/10.1103/PhysRevX.5.031013.
[18] C. Fang, H. Weng, X. Dai, Z. Fang, Topological nodal line semimetals, Chin. Phys. B 25 (2016) 117106, https://doi.org/10.1088/1674-1056/25/11/117106/meta.
[19] C. Zhong, Y. Chen, Y. Xie, S.A. Yang, M.L. Cohen, S. Zhang, Towards three-dimensional Weyl-surface semimetals in graphene networks, Nanoscale 8 (2016) 7232, https://doi.org/10.1039/C6NR00882H.
[20] Z. Wang, A. Alexandradinata, R.J. Cava, B.A. Bernevig, Hourglass fermions, Nature 532 (2016) 189, https://doi.org/10.1038/nature17410.
[21] J. Ma, C. Yi, B. Lv, Z. Wang, S. Nie, L. Wang, L. Kong, Y. Huang, P. Richard, P. Zhang, K. Yaji, K. Kuroda, S. Shin, H. Weng, B.A. Bernevig, Y. Shi, T. Qian, H. Ding, Experimental evidence of hourglass fermion in the candidate nonsymmorphic topological insulator KHgSb, Sci. Adv. 3 (2017) e1602415.
[22] M. Ezawa, Hourglass fermion surface states in stacked topological insulators with nonsymmorphic symmetry, Phys. Rev. B 94 (2016) 155148, https://doi.org/10.1103/PhysRevB.94.155148.
[23] L. Wang, S.K. Jian, H. Yao, Hourglass semimetals with nonsymmorphic symmetries in three dimensions, Phys. Rev. B 96 (2017) 165143, https://doi.org/10.1103/PhysRevB.96.075110.
[24] L. Wu, F. Tang, X. Wan, Exhaustive list of topological hourglass band crossings in 230 space groups, Phys. Rev. B 102 (2020) 035106, https://doi.org/10.1103/PhysRevB.102.035106.
[25] W. Wu, Y. Jiao, S. Li, X. Sheng, Z. Yu, S.A. Yang, Hourglass Weyl loops in two dimensions: Theory and material realization in monolayer GaTeI family, Phys. Rev. Mater. 3 (2019) 054203, https://doi.org/10.1103/PhysRevMaterials.3.054203.
[26] Z.F. Wang, B. Liu, W. Zhu, Hourglass fermion in two-dimensional material, Phys. Rev. Lett. 123 (2019) 126403, https://doi.org/10.1103/PhysRevLett.123.126403.
[27] N. Marzari, D. Vanderbilt, Maximally localized generalized Wannier functions for composite energy bands, Phys. Rev. B 56 (1997) 12847, https://doi.org/10.1103/PhysRevB.56.12847.
[28] K. Wang, Y. Li, H. Mei, P. Li, Z.X. Guo, Quantum anomalous Hall and valley quantum anomalous Hall effects in two-dimensional d^0 orbital XY monolayers, Phys. Rev. Mater. 6 (2022) 044202, https://doi.org/10.1103/PhysRevMaterials.6.044202.
[29] G. Kresse, J. Hafner, Ab initio molecular dynamics for liquid metals, Phys. Rev. B 47 (1993) 558, https://doi.org/10.1103/PhysRevB.47.558.
[30] G. Kresse, D. Joubert, From ultrasoft pseudopotentials to the projector augmented-wave method, Phys. Rev. B 59 (1999) 1758, https://doi.org/10.1103/PhysRevB.59.1758.
[31] P.E. Blöchl, Projector augmented-wave method, Phys. Rev. B 50 (1994) 17953, https://doi.org/10.1103/PhysRevB.50.17953.
[32] A. Togo, F. Oba, I. Tanaka, First-principles calculations of the ferroelastic transition between rutile-type and $CaCl_2$-type SiO_2 at high pressures, Phys. Rev. B 78 (2008) 134106, https://doi.org/10.1103/PhysRevB.78.134106.
[33] S.L. Dudarev, G.A. Botton, S.Y. Savrasov, C.J. Humphreys, A.P. Sutton, Electron-energy-loss spectra and the structural stability of nickel oxide: An LSDA+ U study, Phys. Rev. B 57 (1998) 1505, https://doi.org/10.1103/PhysRevB.57.1505.
[34] A.A. Mostofi, J.R. Yates, Y.-S. Lee, I. Souza, D. Vanderbilt, N. Marzari, wannier90: A tool for obtaining maximally-localised Wannier functions, Comput. Phys. Commun. 178 (2008) 685, https://doi.org/10.1016/j.cpc.2007.11.016.

[35] M.P.L. Sancho, J.M.L. Sancho, J. Rubio, Quick iterative scheme for the calculation of transfer matrices: Application to Mo (100), J. Phys. F 14 (1984) 1205, https://doi.org/10.1088/0305-4608/14/5/016/meta.

[36] K. Hirakawa, H. Kadowaki, K. Ubukoshi, Study of frustration effects in two-dimensional triangular lattice antiferromagnes-neutron powder diffraction study of VX_2, X=Cl, Br and I, J. Phys. Soc. Jpn. 52 (1983) 1814, https://doi.org/10.1143/JPSJ.52.1814.

[37] Q.S. Wu, S.N. Zhang, H.F. Song, M. Troyer, A.A. Suluyanov, WannierTools: An open-source software package for novel topological materials, Comput. Phys. Commun. 224 (2018) 405, https://doi.org/10.1016/j.cpc.2017.09.033.

[38] I.S. Novikov, K. Gubaev, E.V. Podryabinkin, A.V. Shapeev, The MLIP package: Moment tensor potentials with MPI and active learning, Mach. Learn. Sci. Technol. (2020), https://doi.org/10.1088/2632-2153/abc9fe.

[39] B. Mortazavi, B. Javvaji, F. Shojaei, T. Rabczuk, A.V. Shapeev, X. Zhuang, Exceptional piezoelectricity, high thermal conductivity and stiffness and promising photocatalysis in two-dimensional $MoSi_2N_4$ family confirmed by first-principles, Nano Energy 82 (2021) 105716, https://doi.org/10.1016/j.nanoen.2020.105716.

[40] J.Y. You, B. Gu, G. Su, The p-orbital magnetic topological states on a square lattice, Nat. Sci. Rev. 9 (2022) nwab114, https://doi.org/10.1093/nsr/nwab114.

[41] S.S. Wang, Y. Liu, Z.M. Yu, X.L. Sheng, S.A. Yang, Hourglass Dirac chain metal in rhenium dioxide, Nat. Commun. 8 (2017) 1844, https://doi.org/10.1038/s41467-017-01986-3.